



# High-valent cobalt active sites derived from electrochemical activation of metal-organic frameworks for efficient nitrate reduction to ammonia

Jinyan Yang<sup>a,1</sup>, Wen-Da Zhang<sup>a,1</sup>, Han Zhao<sup>b,1</sup>, Yizhong Zou<sup>a</sup>, Ze-Yi Zhang<sup>b</sup>, Jiangyong Liu<sup>c</sup>, Jing Wang<sup>a,\*</sup>, Zhi-Guo Gu<sup>a</sup>, Xiaodong Yan<sup>a,\*</sup>

<sup>a</sup> Key Laboratory of Synthetic and Biological Colloids, Ministry of Education, School of Chemical and Material Engineering Jiangnan University, Wuxi 214122, PR China

<sup>b</sup> Department of Chemistry, University of Zurich, Winterthurerstrasse 190, CH-8057 Zurich, Switzerland

<sup>c</sup> School of Chemistry and Chemical Engineering, Yangzhou University, Yangzhou 225002, PR China

## ARTICLE INFO

### Keywords:

Electroreduction of nitrate to ammonia  
Metal-organic frameworks  
Structural reconstruction  
Electrochemical activation  
Operando technology

## ABSTRACT

Metal-organic frameworks (MOFs) exhibited great potential in the electrocatalytic reduction of nitrate to ammonia (eNO<sub>3</sub>RR), but the structural transformation and the identification of the active sites in the electrochemical process have rarely been reported. Herein, a series of MOFs have been fabricated for eNO<sub>3</sub>RR. The Co-based MOF (Co-TPA) is selected as a representative for exploration through *in-situ* and *ex-situ* techniques to reveal the structural evolution during eNO<sub>3</sub>RR. The structural transformation from the Co-TPA to electrochemically activated catalyst (Co-TPA-E) is verified, and it is found that the *in-situ* formed high-valent Co species (CoOOH) are the active sites for eNO<sub>3</sub>RR. Moreover, the formation of the high-valence CoOOH species can be further facilitated by introducing highly electronegative Cu ions into the Co-TPA-E, resulting in excellent catalytic activity with an NH<sub>3</sub> yield rate of 1.12 mmol h<sup>-1</sup> cm<sup>-2</sup> at -0.326 V vs. RHE and a maximum Faradaic efficiency of 99.62 %.

## 1. Introduction

Ammonia (NH<sub>3</sub>), as one of the world's most intensively produced chemicals, is widely used in various fields such as dye, medicine, and fertilizer production [1,2]. Meanwhile, NH<sub>3</sub> is a renewable carbon-free energy carrier with high energy density and hydrogen content (17.6 wt% hydrogen) [3,4]. The industrial synthesis of NH<sub>3</sub> still relies on the Haber-Bosch route, which has high energy consumption and high emission of CO<sub>2</sub> greenhouse gas [5,6]. Recently, electrochemical synthesis of ammonia has aroused wide interest [7–10]. Among them, the electrocatalytic reduction of nitrate to ammonia (eNO<sub>3</sub>RR) is considered as a feasible way due to the lower N = O bond energy (204 kJ mol<sup>-1</sup>) and higher solubility of NO<sub>3</sub> than N<sub>2</sub> [11,12]. In addition, nitrate is also a contaminant, which widely exists in agricultural and industrial wastewater [12]. Therefore, from energy and environmental aspects, eNO<sub>3</sub>RR not only produces high-value ammonia but also alleviates water pollution, achieving the purpose of "turning waste into treasure". Nonetheless, the eNO<sub>3</sub>RR is a complex reaction involving eight electron transfer and various by-products (such as NO<sub>2</sub>, N<sub>2</sub>H<sub>4</sub>, etc.), resulting in

limited conversion efficiency [13–16]. Therefore, rational design of electrocatalysts with high activity and selectivity is the key to achieving highly efficient eNO<sub>3</sub>RR.

Metal-organic frameworks (MOFs) are linked by metal ions and organic ligands, showing great potential in the field of electrocatalysis due to their porous structure, tuneable electronic property, and abundant metal sites [17,18]. On one hand, MOFs can directly serve as electrocatalysts to drive the eNO<sub>3</sub>RR [19–24]. For example, Liu group reported the preparation of a stable MOFs, which displayed high chemical stability and a Faradaic efficiency of 94.7 % [24]. However, the overall catalytic performance of the MOFs is limited due to their low conductivity. On the other hand, meta-stable MOFs undergo structural reconstruction under electrochemical conditions, and thus MOFs are not the real catalysts [25,26]. The reconstruction of the meta-stable MOFs usually generates inorganic materials, such as hydroxides [27], which have better conductivity and more active sites than the MOFs. Recently, a Cu/Pd/CuO<sub>x</sub> multi-phase heterostructure was fabricated through the reconstruction of the Pd-incorporated Cu-based MOFs, which delivered a high ammonia production rate of 1510.3 μg h<sup>-1</sup> mg<sub>catalyst</sub><sup>-1</sup> due to the

\* Corresponding authors.

E-mail addresses: [jingwang@jiangnan.edu.cn](mailto:jingwang@jiangnan.edu.cn) (J. Wang), [xiaodong.yan@jiangnan.edu.cn](mailto:xiaodong.yan@jiangnan.edu.cn) (X. Yan).

<sup>1</sup> These authors contributed equally to this work.

electronic interaction between the *in-situ* formed multi-phase species [28]. This result indicates that *in-situ* reconstruction of the unstable MOFs is an effective strategy to prepare highly active eNO<sub>3</sub>RR catalysts. However, to the best of our knowledge, the structural transformation process of the MOFs and the identification of the actual active sites of the MOFs-derived materials have rarely been reported for eNO<sub>3</sub>RR.

Herein, we synthesized a series of MOFs using terephthalic acid (TPA) and different metals for eNO<sub>3</sub>RR, all of which underwent *in-situ* activation process under nitrate electroreduction operating conditions (Fig. 1). The Co-based MOF (Co-TPA) was selected as a representative to reveal its structural evolution during the eNO<sub>3</sub>RR. The structural transformation from the Co-TPA to the electrochemically activated catalyst (Co-TPA-E) was well demonstrated by *ex-situ* X-ray absorption spectroscopy (XAS) and X-ray diffraction (XRD). Moreover, operando techniques such as electrochemical impedance spectroscopy (EIS) and Raman spectroscopy unveiled that the *in-situ* formation of the high-valent Co species during the eNO<sub>3</sub>RR. Noticeably, the eNO<sub>3</sub>RR activity can be further boosted by incorporating the highly electronegative Cu ions into the Co-TPA-E (CuCo-TPA-E). The CuCo-TPA-E displayed excellent eNO<sub>3</sub>RR performance with an NH<sub>3</sub> yield rate of 1.12 mmol h<sup>-1</sup> cm<sup>-2</sup> at -0.326 V vs. RHE. Finally, the X-ray photoelectron spectroscopy (XPS), Raman spectroscopy, and theoretical calculations showed that the introduction of Cu ions adjusted the electron cloud distribution at the Co active sites and further enhanced the NO<sub>3</sub><sup>-</sup> adsorption and the NH<sub>3</sub> desorption on the Co sites. When used as a cathode in a rechargeable Zn-NO<sub>3</sub> battery, the CuCo-TPA-E achieves a power density of 8.46 mW cm<sup>-2</sup>.

## 2. Experimental section

### 2.1. Preparation of the M-TPA

In a typical synthesis process, a piece of carbon paper (1 cm × 2 cm) was firstly cleaned ultrasonically in water and ethanol for 10 min, respectively. Then, 0.5 mmol of TPA was dissolved in 7.0 mL of N,N-Dimethylformamide under ultrasonic agitation for 10 min. After that, 0.5 mmol of CoCl<sub>2</sub>•6 H<sub>2</sub>O, 1.0 mL of ethanol, and 1.0 mL of deionized water were sequentially added into the above solution. The solution and a piece of the cleaned carbon paper were transferred into a Teflon-lined stainless autoclave for hydrothermal reaction at 120 °C for 12 h in an electric oven. After the autoclave was cooled down to room temperature, the precursor was taken out, washed with deionized water and ethanol for several times, and dried. The precursor is named as Co-TPA. The Cu-TPA, Ni-TPA, Fe-TPA and CuCo-TPA (Cu<sup>2+</sup>:Co<sup>2+</sup>=1:1) were synthesized by the same synthesis procedures using different metal salts.

### 2.2. Electrochemical activation of the M-TPA

The electrochemical activation was conducted on a CHI760E electrochemistry workstation. The Co-TPA was activated in 1.0 M KOH + 0.1 M KNO<sub>3</sub> at -0.326 V vs. RHE for 10 min. Then, the sample were gently washed with water and acetone, and dried. The obtained product is named as Co-TPA-E. The Cu-TPA, Fe-TPA, Ni-TPA, and CuCo-TPA were activated under the same conditions. The activated Cu-TPA, Fe-TPA, Ni-TPA, and CuCo-TPA were named as Cu-TPA-E, Fe-TPA-E, Ni-TPA-E, and CuCo-TPA-E, respectively.

## 3. Results and discussion

### 3.1. Synthesis and characterization of the Co-TPA and Co-TPA-E

The Co-TPA was grown on carbon paper in a one-step solvothermal process. Its crystal structure was verified by the XRD pattern (Fig. S1). Then, the Co-TPA-E was obtained through electrochemical activation of the Co-TPA at -0.326 V vs. RHE in 1.0 M KOH + 0.1 M KNO<sub>3</sub>. The electrochemical activation process was monitored by the current density. As shown in Fig. S2, the current density increased with activation time, indicating that the Co-TPA underwent structural transformation, and then remained constant after 600 s, suggesting that the activation/reconstruction of the Co-TPA was completed. Linear sweep voltammetry (LSV) measurement was conducted at different activation times to further monitor the activation process. As shown in Fig. 2a, the current density of the Co-TPA-E (600 s) is nearly twice larger than that of the pristine Co-TPA at -0.4 V vs. RHE. When the activation time prolonged to 700 and 800 s, the LSV curves show no significant change (Fig. S3), confirming that the structural reconstruction occurred within the initial 600 s.

The structural evolution from Co-TPA to Co-TPA-E was studied by *in-situ* Raman spectra (Fig. 2b). At the initial stage, the signals from the TPA ligand were observed at 630, 856, 1121, 1410 and 1611 cm<sup>-1</sup> [29]. After the activation of 200 s, two new peaks at 423 and 503 cm<sup>-1</sup> were observed, which corresponded to the Co-O of the Co(OH)<sub>2</sub> and CoOOH, respectively [30–32]. This indicated the *in-situ* generation of the Co-TPA derived inorganic materials. When the activation time exceeded 400 s, the characteristic peaks from the Co-TPA disappeared, showing only two peaks at 423 and 503 cm<sup>-1</sup>, indicating that the Co-TPA was fully converted into (oxy)hydroxide. As the activation time prolonged, the signal at 503 cm<sup>-1</sup> became stronger, suggesting that more and more CoOOH species were formed.

Operando EIS is a useful experimental tool in probing the kinetics of the electrocatalytic reaction and the properties of the electrode/electrolyte interfaces [33,34]. As shown in Fig. 2c, the Bode plots at -0.326 V vs. RHE at different activation times were recorded, in which the high-frequency peak can be attributed to the electric double-layer

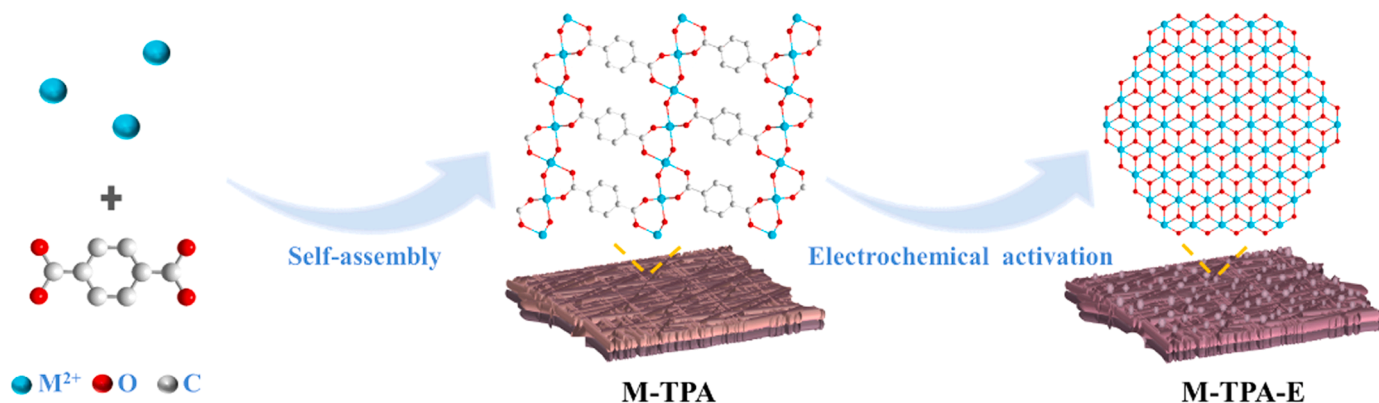
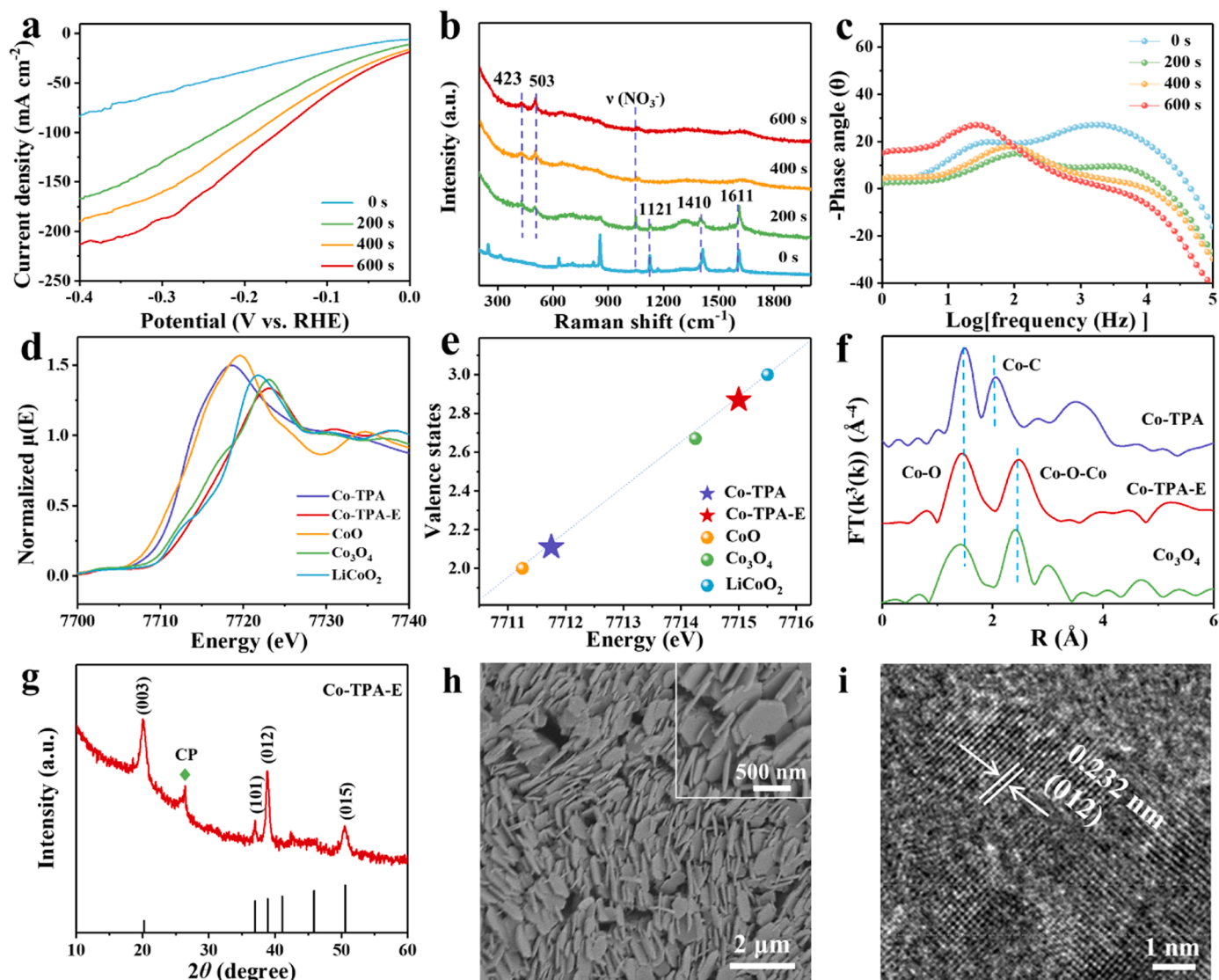


Fig. 1. Schematic illustration of the preparation process of the M-TPA and M-TPA-E (M = Co, Cu, Ni, Fe and CuCo).



**Fig. 2.** The (a) LSV curves, (b) in-situ Raman spectra and (c) Bode phase plots of the Co-TPA activated at  $-0.326$  V vs. RHE for different times ( $t = 0, 200, 400$  and  $600$  s). The (d) Co K-edge XANES spectra and (e) calculated Co valence states of the Co-TPA, Co-TPA-E, CoO,  $\text{Co}_3\text{O}_4$  and  $\text{LiCoO}_2$ . (f) The EXAFS spectra of the Co-TPA, Co-TPA-E and  $\text{Co}_3\text{O}_4$ . (g) The XRD pattern of the Co-TPA-E. The (h) SEM and (i) HRTEM images of the Co-TPA-E.

capacitance and the low-frequency peak is related to the nonhomogeneous charge distribution ( $C_{\text{ads}}$ ) [35,36]. The phase angle in the high frequency region decreases with activation time, indicating that the conductivity of the catalyst increases with activation time. This means that the *in-situ* generated (oxy)hydroxide has higher conductivity than the Co-TPA. The phase angle corresponding to the  $C_{\text{ads}}$  increases with activation time, suggesting that the *in-situ* generated (oxy)hydroxide can promote the adsorption of the reaction intermediates and accelerate the reaction kinetics of  $\text{eNO}_3\text{RR}$ .

The *ex-situ* XAS technique was adopted to explore the change in the electronic structure and valence state of the catalyst before and after the electrochemical activation [37]. As shown by the Co K-edge X-ray absorption near edge structure (XANES) spectra in Fig. 2d, the white line of the Co-TPA-E positively shifted as compared with that of the Co-TPA, implying the increase in valence state of the Co after structural reconstruction [38]. The absorption edge of the Co-TPA is close to that of the CoO, while the one of the Co-TPA-E is between those of the  $\text{Co}_3\text{O}_4$  and  $\text{LiCoO}_2$ . In addition, we acquired the Co oxidation state as a function of Co K-edge energy shift [39,40]. The valence state of the Co is close to  $+3$  (Fig. 2e), which is in accordance with the XPS data (Fig. S4). Further, the structure of the Co-TPA and Co-TPA-E were studied by the

extended X-ray absorption fine-structure (EXAFS) spectroscopy. The two main peaks of the Co-TPA at  $1.47$  and  $2.05$  Å can be ascribed to the Co–O and Co–C coordination, respectively (Fig. 2f). After electrochemical activation, the peak of the Co–C disappeared, and a new peak at  $2.46$  Å from the Co–O–Co was observed, indicating the complete reconstruction of the Co-TPA.

As shown in Fig. 2g, the X-ray diffraction peaks at  $20.2^\circ$ ,  $36.9^\circ$ ,  $38.8^\circ$  and  $50.5^\circ$  are observed for the Co-TPA-E, which are indexed to the (003), (101), (012) and (015) crystal planes of the  $\text{CoOOH}$  (PDF No. 07-0169), respectively. The scanning electron microscopy (SEM) images show that the Co-TPA has layered structure (Fig. S5a) and that the Co-TPA-E present in the form of hexagonal nanosheets with a size of  $20$  nm in thickness (Figs. 2h and S5b), which is further confirmed by the transmission electron microscopy (TEM) image (Fig. S6a). The high-resolution TEM (HRTEM) images demonstrate the lattice fringe of the Co-TPA-E (Figs. 2i and S6b). The  $d$ -spacing of  $0.232$  nm (Fig. 2i) matches well with the interplanar distance of the (012) facets of  $\text{CoOOH}$ . The energy dispersive X-ray (EDX) mapping images show the homogeneous distribution of the Co and O elements in the whole nanosheet (Fig. S7). It is thus concluded that the  $\text{CoOOH}$  was successfully synthesized by *in-situ* electrochemical activation of the Co-TPA.

### 3.2. Electrocatalytic performance and mechanism study of the Co-TPA-E towards $\text{eNO}_3\text{RR}$

The  $\text{eNO}_3\text{RR}$  performance of the Co-TPA-E was evaluated using a three-electrode system of an H-type electrolytic cell. The colorimetric method was employed to detect the concentration of the  $\text{NH}_3$  in the electrolyte (Figs. S8 and S9) [4]. According to the LSV curves of the Co-TPA-E (Fig. 3a and S10), the current density ( $190.2 \text{ mA cm}^{-2}$ ) in  $1.0 \text{ M KOH} + 0.1 \text{ M KNO}_3$  is nearly 10-fold that ( $19.2 \text{ mA cm}^{-2}$ ) in  $1.0 \text{ M KOH}$  at  $-0.326 \text{ V}$  vs. RHE. This indicates that the Co-TPA-E can efficiently drive the  $\text{eNO}_3\text{RR}$ . Further, we synthesized the Cu-TPA-E, Ni-TPA-E and Fe-TPA-E for the  $\text{eNO}_3\text{RR}$  (Figs. S11–S13). As shown in Fig. 3b and Fig. 3c, the Cu-TPA-E exhibited the best electrochemical performance in view of the current density and Tafel slope, but moderate  $\text{NH}_3$  yield rate (Fig. 3d). From the perspective of Faradaic efficiency, the Co-TPA-E is the best among all the catalysts, suggesting that the Co-TPA-E has the highest selectivity to  $\text{NH}_3$  (Fig. S14). In addition, the Co-TPA-E possesses higher catalytic performance than the Ni-TPA-E and Fe-TPA-E. The Co-TPA-E required a potential of  $0.01 \text{ V}$  vs. RHE to deliver a current density of  $10 \text{ mA cm}^{-2}$ , which was more positive than

the Ni-TPA-E ( $-0.09 \text{ V}$  vs. RHE) and Fe-TPA-E ( $-0.082 \text{ V}$  vs. RHE). Also, the Co-TPA-E displayed a lower Tafel slope of  $138 \text{ mV dec}^{-1}$  than the Ni-TPA-E ( $292 \text{ mV dec}^{-1}$ ) and Fe-TPA-E ( $329 \text{ mV dec}^{-1}$ ), reflecting faster  $\text{eNO}_3\text{RR}$  kinetics. Moreover, the Co-TPA-E exhibited an  $\text{NH}_3$  yield rate of  $0.91 \text{ mmol h}^{-1} \text{ cm}^{-2}$  at  $-0.376 \text{ V}$  vs. RHE, which is far higher than the Ni-TPA-E ( $0.0476 \text{ mmol h}^{-1} \text{ cm}^{-2}$ ) and Fe-TPA-E ( $0.598 \text{ mmol h}^{-1} \text{ cm}^{-2}$ ). The Faradaic efficiency of the Co-TPA-E at different potentials was further studied via the potentiostatic method. As displayed in Fig. 3e, the Faradaic efficiency increased steadily and reached the maximum value of  $99.61\%$  at  $-0.326 \text{ V}$  vs. RHE (Fig. S15). Nuclear magnetic resonance (NMR) is further used to verify the concentration of  $\text{NH}_4^+$ , which is consistent with the result of the colorimetric method (Figs. 3f, S16, and S17). Further, another possible liquid by-product ( $\text{N}_2\text{H}_4$ ) was analyzed, and no obvious signal was detected (Fig. S18). The stability of the Co-TPA-E was investigated at  $-0.326 \text{ V}$  vs. RHE. The Faradaic efficiency and ammonia yield did not decrease significantly during the 15 continuous cycle tests, confirming its excellent electrocatalytic stability (Fig. S19). These results demonstrate the good catalytic performance of the Co-TPA-E towards  $\text{eNO}_3\text{RR}$ .

*In-situ* Raman technique was used to probe the structural evolution of

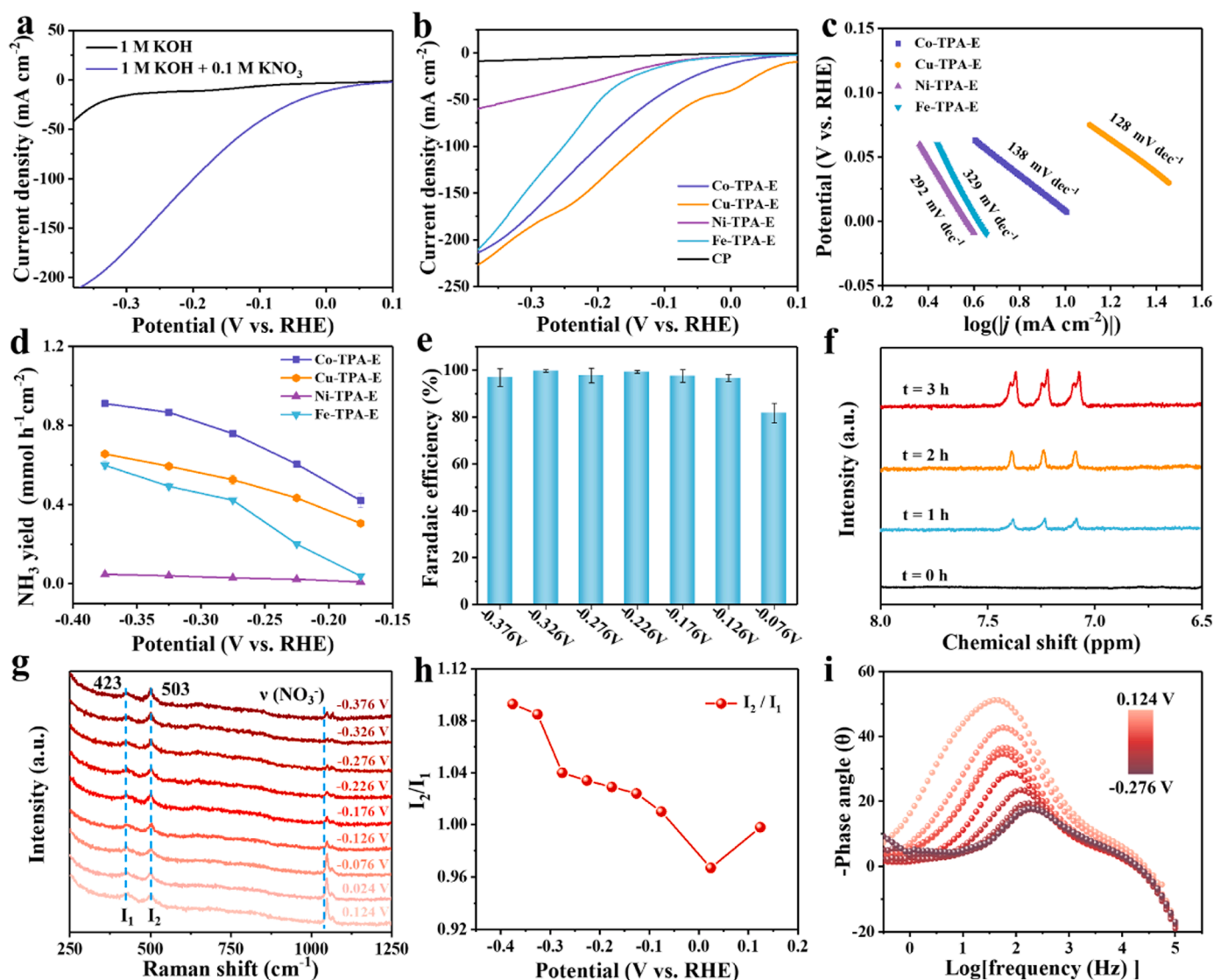


**Fig. 3.** (a) The LSV curves of the Co-TPA-E in  $1 \text{ M KOH}$  with and without the presence of  $0.1 \text{ M KNO}_3$ . The (b) LSV curves, (c) Tafel plots and (d)  $\text{NH}_3$  yield rate at different potentials of the electrochemically activated catalysts. (e) The Faradaic efficiency of the Co-TPA-E at different potentials. (f) The  $^1\text{H}$  NMR spectra of the electrolyte tested at 0, 1, 2 and 3 h. The (g) in-situ Raman spectra, (h) ratio of the peak intensities of the  $\text{CoOOH}$  ( $I_2$ ) and  $\text{Co(OH)}_2$  ( $I_1$ ), and (i) Bode plots of the Co-TPA-E at varied potentials.

the catalyst during the  $\text{eNO}_3\text{RR}$ . The intensity of the Raman signal at  $1050\text{ cm}^{-1}$  corresponding to nitrate ions decreased when the applied potential decreased, implying the occurrence of the reduction of nitrate ions [29]. In addition, the signals at  $503\text{ cm}^{-1}$  ( $\text{I}_2$ ) and  $423\text{ cm}^{-1}$  ( $\text{I}_1$ ) assigned to the  $\text{CoOOH}$  and  $\text{Co}(\text{OH})_2$ , respectively were further analyzed (Fig. 3g) [30,32]. As shown in Fig. 3h and Fig. S20, the  $\text{I}_2/\text{I}_1$  ratio decreased from 1.0 to 0.96 when the potential changed from 0.124 to 0.024 V vs. RHE, indicating the partial reduction of the  $\text{CoOOH}$  into  $\text{Co}(\text{OH})_2$ . Interestingly, the  $\text{I}_2/\text{I}_1$  ratio increased with further negatively shifting the potential, and it reached 1.1 at  $-0.376\text{ V}$  vs. RHE, indicating that the  $\text{CoOOH}$  is the active sites for  $\text{eNO}_3\text{RR}$ . We propose that the in-situ formed  $\text{CoOOH}$  is related with the oxidative species from the  $\text{eNO}_3\text{RR}$ , which is consistent with the literature [32,41]. Control experiment was conducted in 1.0 M KOH without  $\text{KNO}_3$ . The electrochemical properties of the catalyst did not change after electrochemical activation in 1.0 M KOH (Fig. S21). Also, the Raman signals showed no obvious change after electrochemical activation in 1.0 M KOH (Fig. S22), which further demonstrates that the formation of  $\text{CoOOH}$  was caused by  $\text{eNO}_3\text{RR}$ .

The Nyquist plots were measured at different potentials from 0.124 to  $-0.276\text{ V}$  vs. RHE (Fig. 3i), which was used to describe the reaction kinetics on the surface of the catalyst [42–44]. The Co-TPA-E exhibited low series resistance values at different potentials (Fig. S23), which agree well with its fast reaction kinetics. In addition, the EIS spectra of the Co-TPA-E show that the diameter of the semicircle corresponding to the charge transfer resistance ( $R_{ct}$ ) decreases with decreasing the potential, indicating the enhanced  $\text{eNO}_3\text{RR}$ . Furthermore, the phase peak of the Co-TPA-E decreases with decreasing the potential in the high-frequency region. This shows that the  $\text{eNO}_3\text{RR}$  performance is more kinetically favorable at more negative potential, which agrees well with the Faradaic efficiency and  $\text{NH}_3$  yield rate of the Co-TPA-E.

### 3.3. Electrocatalytic performance of the CuCo-TPA-E towards $\text{eNO}_3\text{RR}$

We have proved that the high-valence Co centers are the active sites by in-situ Raman characterization (Figs. 3g and 3h). Hence, we speculate that promoting the valence state of the Co centers may further enhance the  $\text{eNO}_3\text{RR}$  performance. With that in mind, we introduce the more electronegative Cu into the Co-TPA [45]. The XRD pattern of the CuCo-TPA is similar to that of the Co-TPA (Fig. S24), indicating the formation of the isomorphous CuCo-TPA. Also, its morphology is similar to that of the Co-TPA (Fig. S25). The CuCo-TPA-E was obtained by the above-mentioned electrochemical activation process. The XRD, HRTEM, and Raman measurements (Fig. S26) show that the CuCo-TPA-E is Cu-doped  $\text{CoOOH}$ . As shown by the LSV curves in Fig. 4a, the CuCo-TPA-E has higher current density than the Cu-TPA-E and Co-TPA-E. Specifically, the current density of the CuCo-TPA-E is about two times those of the Co-TPA-E and Cu-TPA-E at  $-0.326\text{ V}$  vs. RHE. In addition, the  $\text{NH}_3$  yield rates of the Co-TPA-E ( $0.869\text{ mmol h}^{-1}\text{ cm}^{-2}$ ) and Cu-TPA-E ( $0.594\text{ mmol h}^{-1}\text{ cm}^{-2}$ ) were much lower than that of the CuCo-TPA-E ( $1.12\text{ mmol h}^{-1}\text{ cm}^{-2}$ ) at  $-0.326\text{ V}$  vs. RHE (Fig. 4b). The Faradaic efficiency of the CuCo-TPA-E was more than 90 % from  $-0.176\text{ V}$  to  $-0.326\text{ V}$  vs. RHE (Fig. 4c), which is much higher than that of the Cu-TPA-E, indicating that the introduction of Cu ions did not reduce the Faradaic efficiency. As shown Fig. 4d and Table S1, the CuCo-TPA-E presented outstanding  $\text{eNO}_3\text{RR}$  performance, which is superior to most of the previously reported catalysts (see references in Table S1). The catalyst stability is another crucial factor of the electrocatalysts for practical applications. The consecutive recycling test of 15 cycles at  $-0.276\text{ V}$  vs. RHE were applied to investigate the durability of the CuCo-TPA-E (Fig. 4e). The Faradaic efficiency remained above 95 % and the  $\text{NH}_3$  yield rate showed very limited change, confirming its excellent stability.

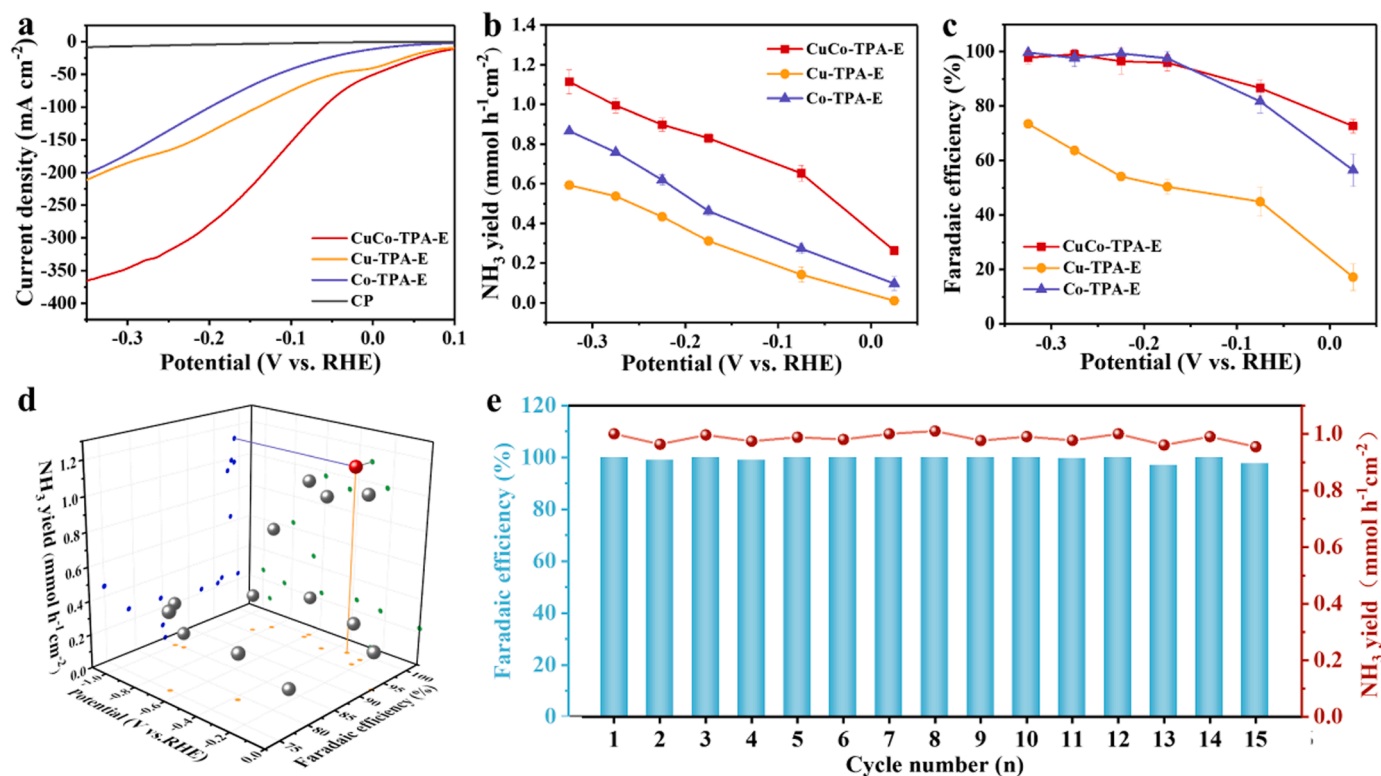


**Fig. 4.** The (a) LSV curves, (b)  $\text{NH}_3$  yield rate and (c) Faradaic efficiency of the Co-TPA-E, Cu-TPA-E and CuCo-TPA-E. (d) Comparison of the performances of the CuCo-TPA-E (Red ball) with the other reported advanced catalysts. (e) Stability tests of the CuCo-TPA-E at  $-0.276\text{ V}$  vs. RHE.

### 3.4. Insights into the reaction mechanism of the CuCo-TPA-E towards eNO<sub>3</sub>RR

To gain insights into the enhanced catalytic activity of the CuCo-TPA-E, *ex-situ* XPS measurement was conducted to identify the surface composition (Figs. 5a and 5b) [46–48]. The Co 2p signals of the CuCo-TPA-E shows a negative shift of 0.7 eV relative to that of the Co-TPA-E, suggesting the increase in valance state of the Co ions after the introduction of Cu ions (Fig. S27 and Table S2) [47]. Also, the Cu 2p signals of the CuCo-TPA-E exhibited a significant negative shift of about 0.7 eV (Table S3). The surface Co/Cu ratio is about 7:3 according to the XPS analysis (Fig. S28). These results indicated that the Cu ions with strong electronegativity adjusted the electronic structure and thus enhanced the valence state of the Co ions, thus improving the catalytic activity. Further, in-situ Raman measurement was used to probe the active phase of the CuCo-TPA-E (Fig. 5c). The peak at 509 cm<sup>-1</sup> corresponding to the CoOOH was observed from 0.124 V to -0.326 V vs. RHE, indicating that the CoOOH centers were the active sites for eNO<sub>3</sub>RR [29,32].

Operando EIS measurements were conducted to explain the improved catalytic kinetics on the CuCo-TPA-E [42–44]. Fig. S29a and S29b show the Nyquist plots of the Co-TPA-E and CuCo-TPA-E at different potentials, respectively. All the Nyquist plots possess one semicircle, indicative of one-time constant model. The larger the diameter of the semicircle, the greater the R<sub>ct</sub>. The R<sub>ct</sub> of both the Co-TPA-E and CuCo-TPA-E decreased with the potential negatively shifting from 0.124 to -0.126 V vs. RHE, and remained constant from -0.176 to -0.326 V vs. RHE (Fig. S29c). Obviously, the R<sub>ct</sub> of the CuCo-TPA-E electrode is lower than that of the Co-TPA-E electrode from 0.124 to -0.126 V vs. RHE, demonstrating faster reaction kinetics on the surface of the CuCo-TPA-E. The Bode phase plots (Fig. S29d) at -0.126 V vs. RHE show that the phase angle of the CuCo-TPA-E is lower than that of the Co-TPA-E, which implies its higher selectivity in eNO<sub>3</sub>RR [42].

Density functional theory (DFT) calculations were conducted to study the adsorption energy of nitrate (reactant) and desorption energy

of ammonia (product) on the surface of the catalysts in eNO<sub>3</sub>RR. The computational structures of the CuCo-TPA-E for nitrate adsorption and ammonia desorption on Co sites and Cu sites are shown in Fig. 5f and Fig. S30, respectively. The DFT calculations show that both the Cu-TPA-E and CuCo-TPA-E are very suitable for the nitrate adsorption (Fig. 5e) and ammonia desorption (Fig. 5f). On the other hand, the Co sites on the CuCo-TPA-E are more favorable for nitrate adsorption and ammonia desorption than the Cu sites. Importantly, the incorporation of the Cu into the crystal structure highly enhanced the nitrate adsorption and ammonia desorption on the Co sites. It is thus concluded that the CuCo-TPA-E, in which partial Co is substituted by Cu, can function as an efficient electrocatalyst for eNO<sub>3</sub>RR.

### 3.5. Electrocatalytic performance of the CuCo-TPA-E in Zn-NO<sub>3</sub> batteries

The Zn-NO<sub>3</sub> battery is highly attractive for simultaneous ammonia production, NO<sub>3</sub> removal, and electricity supply. Given the excellent catalytic activity of the CuCo-TPA-E, we assembled an aqueous Zn-NO<sub>3</sub> battery [49–51]. The Zn-NO<sub>3</sub> battery is composed of a low-cost Zn plate as the anode and a CuCo-TPA-E electrode as the cathode (Fig. 6a). The anode is immersed in 6.0 M KOH electrolyte, while the cathode is immersed in 1.0 M KOH + 0.1 M KNO<sub>3</sub> electrolyte. The two types of electrolytes are physically separated by the Nafion 117 membrane [52]. Fig. 6b displays the discharge curve and the corresponding power density of the Zn-NO<sub>3</sub> battery. The power density of the Zn-NO<sub>3</sub> battery reached the maximum power density of 8.46 mW cm<sup>-2</sup> at 24 mA cm<sup>-2</sup>. The Zn-NO<sub>3</sub> battery exhibits an open circuit voltage of 1.32 V vs. Zn/Zn<sup>2+</sup> (Fig. 6c), which is only 0.55 V lower than the theoretical open circuit voltage of 1.87 V. Notably, the Zn-NO<sub>3</sub> battery achieved a large NH<sub>3</sub> yield rate of 0.223 mmol h<sup>-1</sup> cm<sup>-2</sup> and a high Faradaic efficiency of 95.2 % at 40 mA cm<sup>-2</sup> (Fig. 6d), outperforming most of the reported battery systems in terms of NH<sub>3</sub> yield (Table S4).

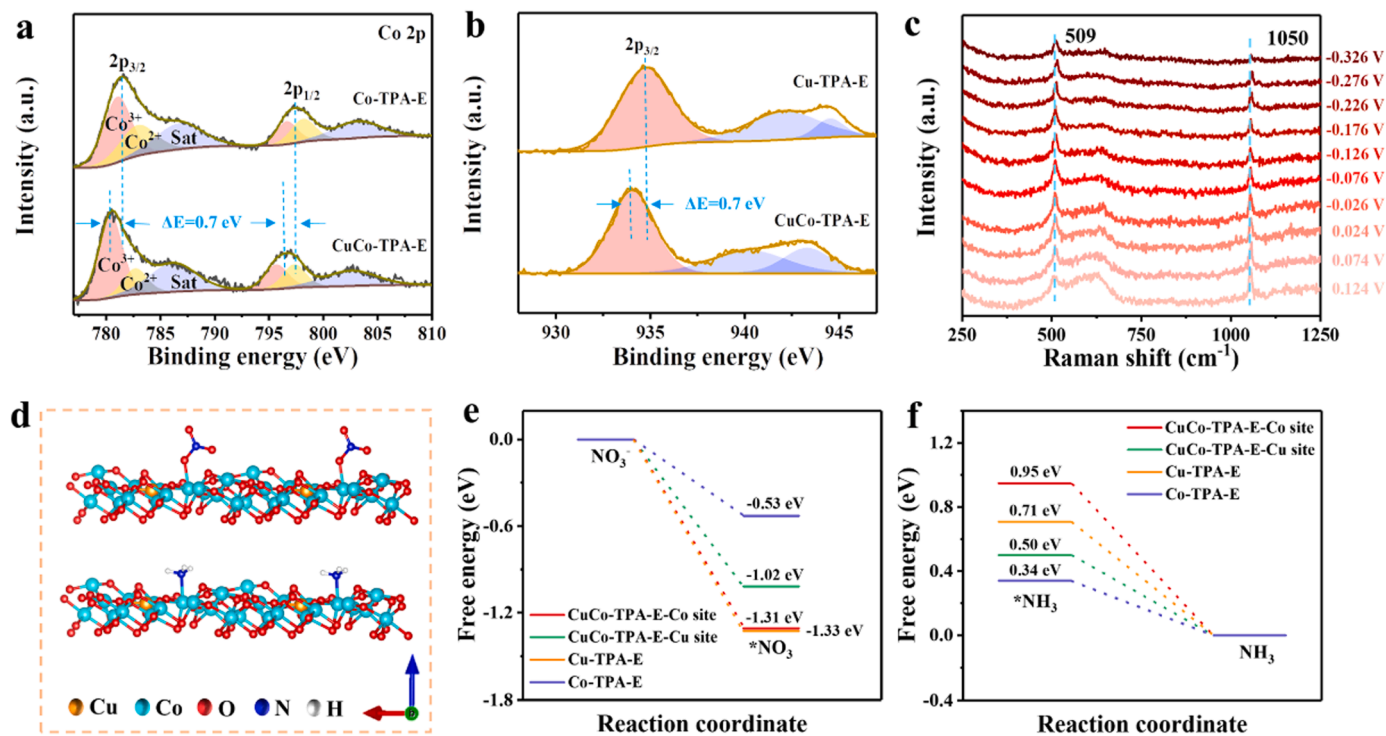


**Fig. 5.** (a) The Co 2p XPS spectra of the Co-TPA-E and CuCo-TPA-E. (b) The Cu 2p XPS spectra of the Cu-TPA-E and CuCo-TPA-E. (c) The in-situ Raman spectra of the CuCo-TPA-E at varied potentials. (d) The computational structures of the CuCo-TPA-E for nitrate adsorption and ammonia desorption on Co sites. The Gibbs free energy for (e) nitrate adsorption and (f) ammonia desorption on the Co-TPA-E, Cu-TPA-E and CuCo-TPA-E (\* represents the active site).

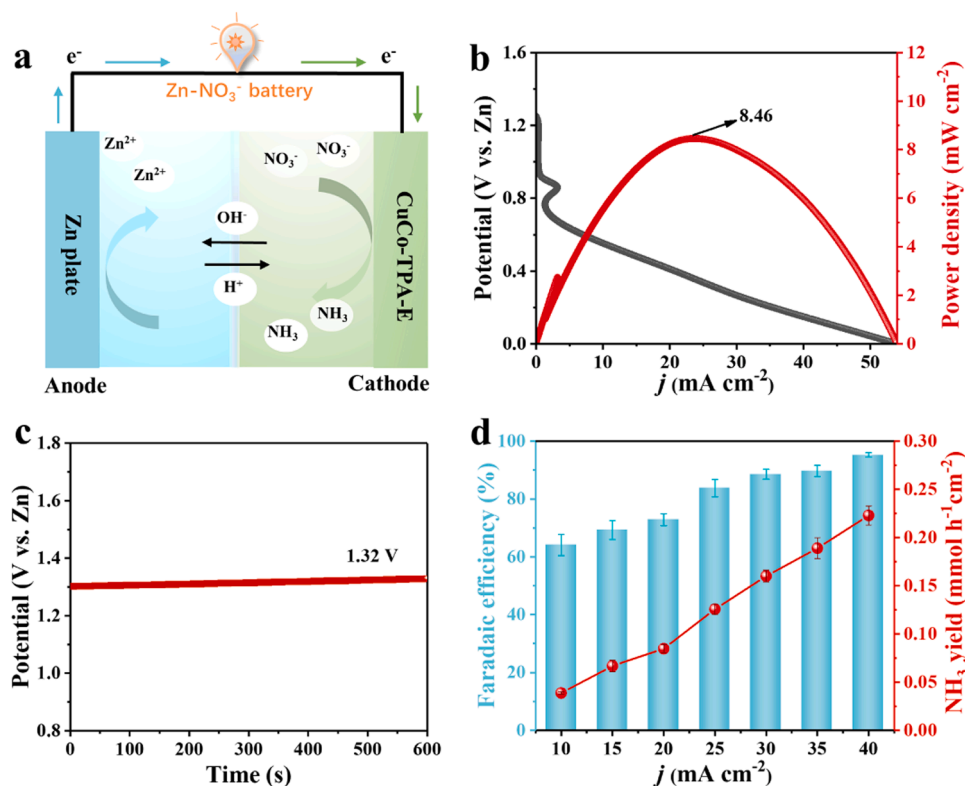


**Fig. 6.** Schematic illustration (a), discharge curve and the corresponding power density (b), and open circuit voltage (c) of the Zn-NO<sub>3</sub> battery. (d) The NH<sub>3</sub> yield rate and Faradaic efficiency of the Zn-NO<sub>3</sub> battery at different current densities.

#### 4. Conclusion

In conclusion, the structural transformation of the Co-TPA and the identification of the active sites in the eNO<sub>3</sub>RR process have been elucidated. The in-situ formed high-valent Co species are revealed to be the active sites for eNO<sub>3</sub>RR. Moreover, the valence state of the Co can be further increased by the introduction of the highly electronegative Cu ions. The electronic interaction between Cu and Co endowed the CuCo-TPA-E with a high NH<sub>3</sub> yield rate of 1.12 mmol h<sup>-1</sup> cm<sup>-2</sup> and a high Faradaic efficiency of 99.62 %, which is superior to both the Co-TPA-E and Cu-TPA-E. *In-situ* Raman, *ex-situ* XPS and theoretical calculations revealed that the introduction of Cu ions tailored the electron cloud distribution and as well enhanced the NO<sub>3</sub><sup>-</sup> adsorption and NH<sub>3</sub> desorption on the Co sites during the eNO<sub>3</sub>RR. The Zn-NO<sub>3</sub> battery using the CuCo-TPA-E electrode as the cathode offered a record-high battery performance. This paper will not only inspire more research on the reconstruction of MOFs in eNO<sub>3</sub>RR, but also open a new avenue to construct novel advanced electrocatalysts for eNO<sub>3</sub>RR.

#### CRediT authorship contribution statement

**Jinyan Yang:** Investigation, Data curation, Writing – original draft. **Wen-Da Zhang:** Investigation, Data curation, Writing – original draft. **Han Zhao:** Computational, Writing – review & editing. **Yizhong Zou:** Investigation, Data curation. **Ze-Yi Zhang:** DFT calculation, Writing – review & editing. **Jiangyong Liu:** Formal analysis, Writing – review & editing. **Jing Wang:** Formal analysis, Writing – review & editing. **Zhi-Guo Gu:** Supervision, Funding acquisition, Writing – review & editing. **Xiaodong Yan:** Investigation, Writing – review & editing, Supervision, Project administration, Funding acquisition.

#### Declaration of Competing Interest

The authors declare that they have no known competing financial

interests or personal relationships that could have appeared to influence the work reported in this paper.

#### Data availability

Data will be made available on request.

#### Acknowledgements

This work was financially supported by the National Natural Science Foundation of China (21905116 and 22075108). Also, we are grateful to the support from the Central Laboratory, School of Chemical and Material Engineering, Jiangnan University.

#### Appendix A. Supporting information

Supplementary data associated with this article can be found in the online version at [doi:10.1016/j.apcatb.2023.123237](https://doi.org/10.1016/j.apcatb.2023.123237).

#### References

- [1] H. Xu, Y. Ma, J. Chen, W.-x. Zhang, J. Yang, Electrocatalytic reduction of nitrate – a step towards a sustainable nitrogen cycle, *Chem. Soc. Rev.* 51 (2022) 2710–2758, <https://doi.org/10.1039/D1CS00857A>.
- [2] C. Wang, Y. Zhang, H. Luo, H. Zhang, W. Li, W.-x. Zhang, J. Yang, Iron-based nanocatalysts for electrochemical nitrate reduction, *Small Methods* 6 (2022), 2200790, <https://doi.org/10.1002/smt.202200790>.
- [3] X. Liang, H. Zhu, X. Yang, S. Xue, Z. Liang, X. Ren, A. Liu, G. Wu, Recent advances in designing efficient electrocatalysts for electrochemical nitrate reduction to ammonia, *Small Struct.* (2022), 2200202, <https://doi.org/10.1002/ssr.202200202>.
- [4] W. Chen, X. Yang, Z. Chen, Z. Ou, J. Hu, Y. Xu, Y. Li, X. Ren, S. Ye, J. Qiu, J. Liu, Q. Zhang, Emerging applications, developments, prospects, and challenges of electrochemical nitrate-to-ammonia conversion, *Adv. Funct. Mater.* (2023), 2300512, <https://doi.org/10.1002/adfm.202300512>.
- [5] Y. Xu, K. Ren, T. Ren, M. Wang, Z. Wang, X. Li, L. Wang, H. Wang, Ultralow-content Pd in-situ incorporation mediated hierarchical defects in corner-etched Cu<sub>2</sub>O octahedra for enhanced electrocatalytic nitrate reduction to ammonia, *Appl.*

- Catal. B Environ. 306 (2022), 121094, <https://doi.org/10.1016/j.apcatb.2022.121094>.
- [6] J. Yu, Y. Qin, X. Wang, H. Zheng, K. Gao, H. Yang, L. Xie, Q. Hu, C. He, Boosting electrochemical nitrate-ammonia conversion via organic ligands-tuned proton transfer, *Nano Energy* 103 (2022), 107705, <https://doi.org/10.1016/j.nanoen.2022.107705>.
  - [7] J. Zhou, F. Pan, Q. Yao, Y. Zhu, H. Ma, J. Niu, J. Xie, Achieving efficient and stable electrochemical nitrate removal by in-situ reconstruction of  $\text{Cu}_2\text{O}/\text{Cu}$  electroactive nanocatalysts on Cu foam, *Appl. Catal. B Environ.* 317 (2022), 121811, <https://doi.org/10.1016/j.apcatb.2022.121811>.
  - [8] F. Jiao, B. Xu, Electrochemical ammonia synthesis and ammonia fuel cells, *Adv. Mater.* 31 (2019), 1805173, <https://doi.org/10.1002/adma.201805173>.
  - [9] Q. Liu, Q. Liu, L. Xie, Y. Ji, T. Li, B. Zhang, N. Li, B. Tang, Y. Liu, S. Gao, Y. Luo, L. Yu, Q. Kong, X. Sun, High-performance electrochemical nitrate reduction to ammonia under ambient conditions using a  $\text{FeOOH}$  nanorod catalyst, *ACS Appl. Mater. Interfaces* 14 (2022) 17312–17318, <https://doi.org/10.1021/acsami.2c00436>.
  - [10] Y. Li, Y.K. Go, H. Ooka, D. He, F. Jin, S.H. Kim, R. Nakamura, Enzyme mimetic active intermediates for nitrate reduction in neutral aqueous media, *Angew. Chem. Int. Ed.* 59 (2020) 9744–9750, <https://doi.org/10.1002/anie.202002647>.
  - [11] Y. Wang, W. Zhou, R. Jia, Y. Yu, B. Zhang, Unveiling the activity origin of a copper-based electrocatalyst for selective nitrate reduction to ammonia, *Angew. Chem. Int. Ed.* 59 (2020) 5350–5354, <https://doi.org/10.1002/anie.201915992>.
  - [12] Y. Wang, H. Li, W. Zhou, X. Zhang, B. Zhang, Y. Yu, Structurally disordered  $\text{RuO}_2$  nanosheets with rich oxygen vacancies for enhanced nitrate electroreduction to ammonia, *Angew. Chem. Int. Ed.* 61 (2022), e202202604, <https://doi.org/10.1002/anie.202202604>.
  - [13] H. Liu, X. Lang, C. Zhu, J. Timoshenko, M. Rüscher, L. Bai, N. Guijarro, H. Yin, Y. Peng, J. Li, Z. Liu, W. Wang, B.R. Cuenya, J. Luo, Efficient electrochemical nitrate reduction to ammonia with copper-supported rhodium cluster and single-atom catalysts, *Angew. Chem. Int. Ed.* 61 (2022), e202202556, <https://doi.org/10.1002/anie.202202556>.
  - [14] F. Du, J. Li, C. Wang, J. Yao, Z. Tan, Z. Yao, C. Li, C. Guo, Active sites-rich layered double hydroxide for nitrate-to-ammonia production with high selectivity and stability, *Chem. Eng. J.* 434 (2022), 134641, <https://doi.org/10.1016/j.cej.2022.134641>.
  - [15] J. Yang, H. Qi, A. Li, X. Liu, X. Yang, S. Zhang, Q. Zhao, Q. Jiang, Y. Su, L. Zhang, J.-F. Li, Z.-Q. Tian, W. Liu, A. Wang, T. Zhang, Potential-driven restructuring of Cu single atoms to nanoparticles for boosting the electrochemical reduction of nitrate to ammonia, *J. Am. Chem. Soc.* 144 (2022) 12062–12071, <https://doi.org/10.1021/jacs.2c02262>.
  - [16] F.-Y. Chen, Z.-Y. Wu, S. Gupta, D.J. Rivera, S.V. Lamberts, S. Pecaut, J.Y.T. Kim, P. Zhu, Y.Z. Finfrook, D.M. Meira, G. King, G. Gao, W. Xu, D.A. Cullen, H. Zhou, Y. Han, D.E. Perea, C.L. Muhich, H. Wang, Efficient conversion of low-concentration nitrate sources into ammonia on a Ru-dispersed Cu nanowire electrocatalyst, *Nat. Nanotechnol.* 17 (2022) 759–767, <https://doi.org/10.1038/s41565-022-01121-4>.
  - [17] Y. Xu, Q. Li, H. Xue, H. Pang, Metal-organic frameworks for direct electrochemical applications, *Coord. Chem. Rev.* 376 (2018) 292–318, <https://doi.org/10.1016/j.ccr.2018.08.010>.
  - [18] W.-D. Zhang, H. Dong, L. Zhou, H. Xu, H.-R. Wang, X. Yan, Y. Jiang, J. Zhang, Z.-G. Gu, Fe single-atom catalysts with pre-organized coordination structure for efficient electrochemical nitrate reduction to ammonia, *Appl. Catal. B Environ.* 317 (2022), 121750, <https://doi.org/10.1016/j.apcatb.2022.121750>.
  - [19] J. Ma, Y. Zhang, B. Wang, Z. Jiang, Q. Zhang, S. Zhuo, Interfacial engineering of bimetallic Ni/Co-MOFs with H-substituted graphdiyne for ammonia electrosynthesis from nitrate, *ACS Nano* 17 (2023) 6687–6697, <https://doi.org/10.1021/acsnano.2c12491>.
  - [20] Y. Lv, S.-W. Ke, Y. Gu, B. Tian, L. Tang, P. Ran, Y. Zhao, J. Ma, J.-L. Zuo, M. Ding, Highly efficient electrochemical nitrate reduction to ammonia in strong acid conditions with  $\text{Fe}_2\text{M}$ -trinuclear-cluster metal-organic frameworks, *Angew. Chem. Int. Ed.* (2023), e20230524, <https://doi.org/10.1002/anie.202305246>.
  - [21] P. Liu, J. Yan, H. Huang, W. Song, Cu/Co bimetallic conductive MOFs: electronic modulation for enhanced nitrate reduction to ammonia, *Chem. Eng. J.* 466 (2023), 143134, <https://doi.org/10.1016/j.cej.2023.143134>.
  - [22] Y. Lv, J. Su, Y. Gu, B. Tian, J. Ma, J.-L. Zuo, M. Ding, Atomically precise integration of multiple functional motifs in catalytic metal-organic frameworks for highly efficient nitrate electroreduction, *JACS Au* 2 (2022) 2765–2777, <https://doi.org/10.1021/jacsau.2c00502>.
  - [23] M. Jiang, J. Su, X. Song, P. Zhang, M. Zhu, L. Qin, Z. Tie, J.-L. Zuo, Z. Jin, Interfacial reduction nucleation of noble metal nanodots on redox-active metal-organic frameworks for high-efficiency electrocatalytic conversion of nitrate to ammonia, *Nano Lett.* 22 (2022) 2529–2537, <https://doi.org/10.1021/acs.nanolett.2c00446>.
  - [24] Y. Zhang, H. Zheng, K. Zhou, J. Ye, K. Chu, Z. Zhou, L. Zhang, T. Liu, Conjugated coordination polymer as a new platform for efficient and selective electroreduction of nitrate into ammonia, *Adv. Mater.* 35 (2023), 2209855, <https://doi.org/10.1002/adma.202209855>.
  - [25] W.-D. Zhang, Q.-T. Hu, L.-L. Wang, J. Gao, H.-Y. Zhu, X. Yan, Z.-G. Gu, In-situ generated Ni-MOF/LDH heterostructures with abundant phase interfaces for enhanced oxygen evolution reaction, *Appl. Catal. B Environ.* 286 (2021), 119906, <https://doi.org/10.1016/j.apcatb.2021.119906>.
  - [26] W.-D. Zhang, H. Yu, T. Li, Q.-T. Hu, Y. Gong, D.-Y. Zhang, Y. Liu, Q.-T. Fu, H.-Y. Zhu, X. Yan, Z.-G. Gu, Hierarchical trimetallic layered double hydroxide nanosheets derived from 2D metal-organic frameworks for enhanced oxygen evolution reaction, *Appl. Catal. B Environ.* 264 (2020), 118532, <https://doi.org/10.1016/j.apcatb.2019.118532>.
  - [27] B. Singh, A. Yadav, A. Indra, Realizing electrochemical transformation of a metal-organic framework pre-catalyst into a metal hydroxide-oxy(hydroxide) active catalyst during alkaline water oxidation, *J. Mater. Chem. A* 10 (2022) 3843–3868, <https://doi.org/10.1039/D1TA09424F>.
  - [28] T. Ren, Z. Yu, H. Yu, K. Deng, Z. Wang, X. Li, H. Wang, L. Wang, Y. Xu, Interfacial polarization in metal-organic framework reconstructed Cu/Pd/CuO<sub>x</sub> multi-phase heterostructures for electrocatalytic nitrate reduction to ammonia, *Appl. Catal. B Environ.* 318 (2022), 121805, <https://doi.org/10.1016/j.apcatb.2022.121805>.
  - [29] O. Abuzalat, H. Tantawy, M. Mokhtar, A. Baraka, Nano-porous bimetallic organic frameworks (Fe/Co)-BDC, a breathing MOF for rapid and capacitive removal of Cr-oxyanions from water, *J. Water Process. Eng.* 46 (2022), 102537, <https://doi.org/10.1016/j.jwpe.2021.102537>.
  - [30] Z. Kou, Y. Yu, X. Liu, X. Gao, L. Zheng, H. Zou, Y. Pang, Z. Wang, Z. Pan, J. He, S. J. Pennycook, J. Wang, Potential-dependent phase transition and Mo-enriched surface reconstruction of  $\gamma\text{-CoOOH}$  in a heterostructured Co-Mo<sub>2</sub>C pre-catalyst enable water oxidation, *ACS Catal.* 10 (2020) 4411–4419, <https://doi.org/10.1021/acscatal.0c00340>.
  - [31] Z. Chen, C.X. Kronawitter, Y.-W. Yeh, X. Yang, P. Zhao, N. Yao, B.E. Koel, Activity of pure and transition metal-modified CoOOH for the oxygen evolution reaction in an alkaline medium, *J. Mater. Chem. A* 5 (2017) 842–850, <https://doi.org/10.1039/C6TA07482K>.
  - [32] W. He, J. Zhang, S. Dieckhöfer, S. Varhade, A.C. Brix, A. Lielpetere, S. Seisel, J.R. C. Unke, W. Schuhmann, Splicing the active phases of copper/cobalt-based catalysts achieves high-rate tandem electroreduction of nitrate to ammonia, *Nat. Commun.* 13 (2022) 1129, <https://doi.org/10.1038/s41467-022-28728-4>.
  - [33] W. Chen, L. Xu, X. Zhu, Y.-C. Huang, W. Zhou, D. Wang, Y. Zhou, S. Du, Q. Li, C. Xie, L. Tao, C.-L. Dong, J. Liu, Y. Wang, R. Chen, H. Su, C. Chen, Y. Zou, Y. Li, Q. Liu, S. Wang, Unveiling the electrooxidation of urea: intramolecular coupling of the N–N bond, *Angew. Chem. Int. Ed.* 60 (2021) 7297–7307, <https://doi.org/10.1002/anie.202015773>.
  - [34] W.-D. Zhang, L. Zhou, Y.-X. Shi, Y. Liu, H. Xu, X. Yan, Y. Zhao, Y. Jiang, J. Zhang, Z.-G. Gu, Dual-atom catalysts derived from a preorganized covalent organic framework for enhanced electrochemical oxygen reduction, *Angew. Chem. Int. Ed.* (2023), e202304412, <https://doi.org/10.1002/anie.202304412>.
  - [35] W. Cai, Y.-F. Jiang, J. Zhang, H. Yang, J. Zhang, C.-Q. Xu, W. Liu, J. Li, B. Liu, Ruthenium/titanium oxide interface promoted electrochemical nitrogen reduction reaction, *Chem. Catal.* 2 (2022) 1764–1774, <https://doi.org/10.1016/j.cheecat.2022.05.009>.
  - [36] J. Li, H.-X. Liu, W. Gou, M. Zhang, Z. Xia, S. Zhang, C.-R. Chang, Y. Ma, Y. Qu, Ethylene-glycol ligand environment facilitates highly efficient hydrogen evolution of Pt/CoP through proton concentration and hydrogen spillover, *Energy Environ. Sci.* 12 (2019) 2298–2304, <https://doi.org/10.1039/C9EE00752K>.
  - [37] C. Lee, K. Shin, C. Jung, P.-P. Choi, G. Henkelman, H.M. Lee, Atomically embedded Ag via electrodeposition boosts oxygen evolution of CoOOH nanosheet arrays, *ACS Catal.* 10 (2020) 562–569, <https://doi.org/10.1021/acscatal.9b02249>.
  - [38] Y. Chen, C. Chen, C. Zheng, S. Dwaraknath, M.K. Horton, J. Cabana, J. Rehr, J. Vinson, A. Dozier, J.J. Kas, K.A. Persson, S.P. Ong, Database of ab initio L-edge X-ray absorption near edge structure, *Sci. Data* 8 (2021) 153, <https://doi.org/10.1038/s41597-021-00936-5>.
  - [39] F.T. Haase, A. Bergmann, T.E. Jones, J. Timoshenko, A. Herzog, H.S. Jeon, C. Rettenmaier, B.R. Cuenya, Size effects and active state formation of cobalt oxide nanoparticles during the oxygen evolution reaction, *Nat. Energy* 7 (2022) 765–773, <https://doi.org/10.1038/s41560-022-01083-w>.
  - [40] S. Kuppam, Y. Xu, Y. Liu, G. Chen, Phase transformation mechanism in lithium manganese nickel oxide revealed by single-crystal hard X-ray microscopy, *Nat. Commun.* 8 (2017) 14309, <https://doi.org/10.1038/ncomms14309>.
  - [41] A. Boughriet, M. Wartel, Evidence for the highly oxidizing properties of  $\text{NO}_2^-$  and  $\text{NO}^+$  ions in organic media. Application to the study of nitrogen oxide/Li cells, *J. Electroanal. Chem.* 362 (1993) 167–176, [https://doi.org/10.1016/0022-0728\(93\)80018-D](https://doi.org/10.1016/0022-0728(93)80018-D).
  - [42] D. Liu, L. Qiao, Y. Chen, P. Zhou, J. Feng, C.C. Leong, K.W. Ng, S. Peng, S. Wang, W.F. Ip, H. Pan, Electrocatalytic reduction of nitrate to ammonia on low-cost manganese-incorporated  $\text{Co}_3\text{O}_4$  nanotubes, *Appl. Catal. B Environ.* 324 (2023), 122293, <https://doi.org/10.1016/j.apcatb.2022.122293>.
  - [43] Y. Wang, Y.-Q. Zhu, Z. Xie, S.-M. Xu, M. Xu, Z. Li, L. Ma, R. Ge, H. Zhou, Z. Li, X. Kong, L. Zheng, J. Zhou, H. Duan, Efficient electrocatalytic oxidation of glycerol via promoted  $\text{OH}^+$  generation over single-atom-bismuth-doped spinel  $\text{Co}_3\text{O}_4$ , *ACS Catal.* 12 (2022) 12432–12443, <https://doi.org/10.1021/acscatal.2c03162>.
  - [44] C. Zhang, J. Xiao, X. Lv, L. Qian, S. Yuan, S. Wang, P. Lei, Hierarchically porous  $\text{Co}_3\text{O}_4/\text{C}$  nanowire arrays derived from a metal-organic framework for high performance supercapacitors and the oxygen evolution reaction, *J. Mater. Chem. A* 4 (2016) 16516–16523, <https://doi.org/10.1039/C6TA06314D>.
  - [45] Y. Tao, S. Fan, X. Li, J. Yang, J. Wang, M.O. Tadé, S. Liu,  $\text{Cu}_x\text{Co}_{3-x}\text{O}_4$  spinel nanofibers for selective oxidation of 5-hydroxymethylfurfural into fuel additives, *ACS Appl. Nano Mater.* 5 (2022) 16564–16572, <https://doi.org/10.1021/acsnanm.2c03656>.
  - [46] J.-C. Dupin, D. Gonbeau, P. Vinatier, A. Levasseur, Systematic XPS studies of metal oxides, hydroxides and peroxides, *Phys. Chem. Chem. Phys.* 2 (2000) 1319–1324, <https://doi.org/10.1039/A908800H>.
  - [47] Z. Deng, C. Ma, Z. Li, Y. Luo, L. Zhang, S. Sun, Q. Liu, J. Du, Q. Lu, B. Zheng, X. Sun, High-efficiency electrochemical nitrate reduction to ammonia on a  $\text{Co}_3\text{O}_4$  nanoarray catalyst with cobalt vacancies, *ACS Appl. Mater. Interfaces* 14 (2022) 46595–46602, <https://doi.org/10.1021/acsnanm.2c12772>.

- [48] Y. Deng, A.D. Handoko, Y. Du, S. Xi, B.S. Yeo, In situ Raman spectroscopy of copper and copper oxide surfaces during electrochemical oxygen evolution reaction: identification of  $\text{Cu}^{\text{III}}$  oxides as catalytically active species, *ACS Catal.* 6 (2016) 2473–2481, <https://doi.org/10.1021/acscatal.6b00205>.
- [49] R. Zhang, Y. Guo, S. Zhang, D. Chen, Y. Zhao, Z. Huang, L. Ma, P. Li, Q. Yang, G. Liang, C. Zhi, Efficient ammonia electrosynthesis and energy conversion through a Zn-nitrate battery by iron doping engineered nickel phosphide catalyst, *Adv. Energy Mater.* 12 (2022), 2103872, <https://doi.org/10.1002/aenm.202103872>.
- [50] H. Jiang, G.-F. Chen, O. Savateev, J. Xue, L.-X. Ding, Z. Liang, M. Antonietti, H. Wang, Enabled efficient ammonia synthesis and energy supply in a zinc–nitrate battery system by separating nitrate reduction process into two stages, *Angew. Chem. Int. Ed.* 62 (2023), e202218717, <https://doi.org/10.1002/anie.202218717>.
- [51] R. Zhang, S. Zhang, Y. Guo, C. Li, J. Liu, Z. Huang, Y. Zhao, Y. Li, C. Zhi, A Zn–nitrite battery as an energy-output electrocatalytic system for high-efficiency ammonia synthesis using carbon-doped cobalt oxide nanotubes, *Energy Environ. Sci.* 15 (2022) 3024–3032, <https://doi.org/10.1039/D2EE00686C>.
- [52] Q. Liu, L. Xie, J. Liang, Y. Ren, Y. Wang, L. Zhang, L. Yue, T. Li, Y. Luo, N. Li, B. Tang, Y. Liu, S. Gao, A.A. Alshehri, I. Shakir, P.O. Agboola, Q. Kong, Q. Wang, D. Ma, X. Sun, Ambient ammonia synthesis via electrochemical reduction of nitrate enabled by  $\text{NiCo}_2\text{O}_4$  nanowire array, *Small* 18 (2022), 2106961, <https://doi.org/10.1002/sml.202106961>.